Science and Technology of Advanced Materials: Methods

ISSN: (Print) (Online) Journal homepage: www.tandfonline.com/journals/tstm20

Development of a method to evaluate strain in weld solidification using in-situ observations with high-brightness synchrotron X-rays

Houichi Kitano, Tomoya Nagira, Fumiyoshi Yoshinaka, Takahiro Sawaguchi, Takayuki Yamashita, Yasuhiro Aoki & Hidetoshi Fujii

To cite this article: Houichi Kitano, Tomoya Nagira, Fumiyoshi Yoshinaka, Takahiro Sawaguchi, Takayuki Yamashita, Yasuhiro Aoki & Hidetoshi Fujii (2024) Development of a method to evaluate strain in weld solidification using in-situ observations with high-brightness synchrotron X-rays, Science and Technology of Advanced Materials: Methods, 4:1, 2403964, DOI: 10.1080/27660400.2024.2403964

To link to this article: https://doi.org/10.1080/27660400.2024.2403964

SCIENCE AND TECHNOLOGY OF ADVANCED MATERIALS: METHODS
2024, VOL. 4, NO. 1, 2403964
https://doi.org/10.1080/27660400.2024.2403964

Taylor & Francis
Taylor & Francis Group

METHODOLOGY, APPARATUS, EXPERIMENTAL DESIGN

OPEN ACCESS   Check for updates

Development of a method to evaluate strain in weld solidification using in-situ observations with high-brightness synchrotron X-rays

Houichi Kitano[a], Tomoya Nagira[a], Fumiyoshi Yoshinaka[a], Takahiro Sawaguchi[a], Takayuki Yamashita[b], Yasuhiro Aoki[b] and Hidetoshi Fujii[b]

[a]Research Center for Structural Materials, National Institute for Materials Science, Tsukuba, Japan; [b]Joining and Welding Research Institute, Osaka University, Osaka, Japan

ABSTRACT

Welding is a crucial joining technique used in various industrial fields. Recently, we developed an in-situ observation technique using high-brightness synchrotron X-rays to observe the formation of weld solidification microstructures. This study proposes a new method to evaluate the strain distribution and strain history of weld solidification zones using time-series in-situ images. The in-situ images were obtained using the beamline at SPring-8, and we employed an Fe-15Mn-10Cr-8Ni-4Si alloy (in mass%) developed for seismic dampers that is prone to solidification cracking during welding. The strain distribution obtained using the proposed method is compared with that calculated using the template matching method, and its effectiveness is verified. The obtained strain distribution corresponds to known findings, showing a consistent distribution regardless of the resolution of the in-situ images. The proposed method is useful for detailed strain evaluations in weld solidification zones and is expected to become a new tool for future research aimed at understanding solidification cracking, residual stress, and residual deformation in welding technologies.

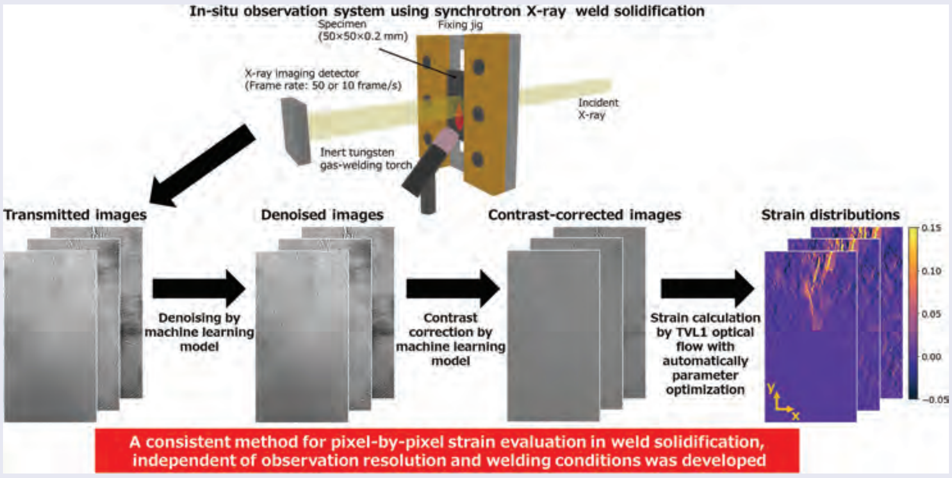

IMPACT STATEMENT

A method was developed to evaluate strain distribution and history in weld solidification using synchrotron X-rays. This method is expected to become a new tool for understanding welding phenomena.

ARTICLE HISTORY
Received 19 June 2024
Revised 15 August 2024
Accepted 9 September 2024

KEYWORDS
Strain evaluation method; in-situ observation; synchrotron X-ray; welding technology; machine learning; optical flow

1. Introduction

Welding is an essential joining technique that forms the basis of various fields, including the manufacturing, construction, and energy industries. Compared with other joining techniques, welding offers significant advantages such as creating strong, lightweight joints with minimal material waste and providing the flexibility to join a wide variety of metallic materials, including those with complex geometries and varying thicknesses. However, welding presents specific challenges. Before welding, metallic materials are typically manufactured with controlled grain size, phase composition, and defect levels to ensure mechanical performance. However, the thermal history

CONTACT Houichi Kitano KITANO.Houichi@nims.go.jp Research Center for Structural Materials, National Institute for Materials Science, 1-2-1, Sengen, Tsukuba 305-0047, Japan

Supplemental data for this article can be accessed online at https://doi.org/10.1080/27660400.2024.2403964

during the welding process can alter these characteristics. Specifically, grain coarsening, phase transformations, and the formation of cracks and defects can occur [1–4]. To deepen our understanding on these issues, we recently developed an in-situ technique using high-brightness synchrotron X-rays for two-dimensional (2D) imaging of the weld solidification microstructural formation process [5–7]. This technology enables the in-situ observation of the solidification microstructure at the micron scale with a high-temporal resolution. Using this developed technology, we visualized crack formation during the welding solidification process which was difficult to observe previously and changes in the solidification mode due to composition adjustments.

This study proposes a new method to evaluate the strain distribution and strain history of weld solidification zones as an additional application of in-situ observation technology. The strain in the weld solidification zone is a crucial factor that causes solidification cracks, welding residual stress, and residual deformation. However, directly evaluating the strain-generation process has been challenging because of the localized concentration and rapid changes in the solidification strain. The proposed strain evaluation method directly assesses the complex and rapidly changing strain distribution using time-series in-situ images.

Typical strain evaluation using time-series images involves noise reduction and contrast correction using classical image processing, such as bilateral filtering [8] and contrast-limited adaptive histogram equalization [9], followed by the calculation of the displacement and strain fields using digital image correlation (DIC) [10] However, preliminary studies have identified several issues when applying the aforementioned procedure to time-series in-situ observation images obtained using high-brightness synchrotron X-ray imaging. First, the appropriate parameters for noise reduction and contrast correction image processing vary depending on the acquisition conditions of the in-situ observation images (welding conditions and image resolution), requiring considerable time for parameter adjustment. Second, in strain evaluations using DIC, a suitable strain distribution may not be calculated owing to the brightness drift, residual noise, and the presence of solid – liquid interfaces in the time-series in-situ images. Therefore, developing a new strain evaluation method is necessary to evaluate the detailed strain behavior in weld solidification zones using time-series in-situ images. This study proposes a new strain evaluation method that combines noise reduction and contrast correction using a machine learning model and strain distribution calculation using the TVL1 optical-flow calculation [11,12]. The proposed method has several advantages:

- Noise reduction and contrast correction of in-situ observation images obtained under different welding conditions and resolutions are possible using the same machine learning model structure
- The attachment parameter in the TVL1 optical-flow calculation (λ in [12]), which affects the results considerably, is now automatically adjusted by an optimization algorithm. This eliminated the need for manual adjustments
- The pixel-by-pixel strain distribution and strain history, which are comparable to the global strain calculated using the template matching method [13], can be calculated

In this study, Fe-15Mn-10Cr-8Ni-4Si alloy [5,14–17] was used as the test material. This alloy was specifically developed for use in seismic dampers but faces the challenge of solidification cracking during welding. Furthermore, there is a strong need to evaluate its strain behavior and to understand the process of solidification crack formation during welding.

2. Experimental methods

2.1. Overview of in-situ observation technique

Figure 1 shows an overview of the in-situ observation system used in this study. Observations were conducted at SPring-8 (beamline number: BL20XU). The energy of the incident X-rays selected for the observations was 28 keV. During tungsten inert gas (TIG) welding, the incident X-rays passed through the sample plate (50 × 50 × 0.2 mm [thickness]) and reached a 2D detector (imaging detector, Hamamatsu photonics, Japan) to capture the transmission image. Simultaneously, visible light images were acquired using a high-speed camera (Nac image technology, Japan). The temperature field was calculated from the visible light images obtained using the two-color method [18] and was used to estimate the molten region (solid – liquid interface).

2.2. Acquisition conditions for in-situ images

An Fe-15Mn-10Cr-8Ni-4Si alloy was used as the test material. In TIG welding, the welding current was 6 A, and pure Ar gas (flow rate 8 L/min) was used as the shielding gas. To obtain time-series in-situ images under different welding conditions and resolutions, in-situ observations were conducted under the three conditions listed in Table 1. The frame rate was set to 50 frames/s for a welding speed of 10 mm/s, and 5 frames/s for a welding speed of 1 mm/s. The high-speed camera captured images at a rate of 250 frames per second under all conditions.

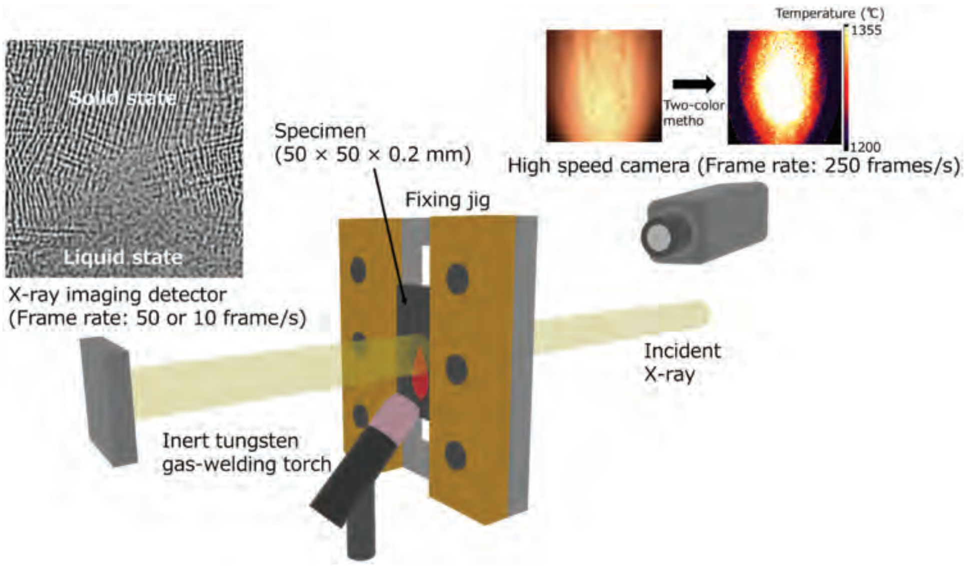

Figure 1. Overview of the in-situ observation system using synchrotron X-rays. The system includes a tungsten inert gas welding setup, where the synchrotron X-ray passes through the sample plate during welding. The transmitted image is captured by a two-dimensional detector, and a high-speed camera simultaneously records visible light images to estimate the temperature distribution using the two-color method.

Table 1. Acquisition conditions for in-situ images. Three different sets of conditions were used to capture time-series images according to variations of the welding speed, resolution, and frame rate. For each condition, the high-speed camera captured images at 250 frames per second.

Test number	Welding speed (mm/s)	Resolution (μm/pixel)	Frate rate (frames/s)
1	10	0.5	50
2	1	0.5	5
3	10	1.1	50

3. Strain evaluation method and verification of effectiveness

3.1. Overview of strain evaluation method

The overall process of the proposed strain evaluation method is illustrated in Figure 2. This method applies three steps to time-series in-situ observations (original images), as shown in the upper, middle, and lower sections of the figure.

The upper section demonstrates the denoising process. This process was executed in three steps: patch splitting, machine learning model processing, and patch merging. Patch splitting and merging procedures are shown in Figure 3. In machine learning model processing, all split images are input into a machine learning model trained for denoising, and the pixel values of the noise-reduced patch images are calculated. The training method for the denoising machine learning model is described in Section 3.2.

The middle section illustrates the contrast correction process. Similar to the denoising process, this process was executed in three steps. In machine learning model processing, a machine learning model trained for contrast correction was used. The training of the machine learning model for contrast correction is described in Section 3.3.

The lower section presents the strain distribution calculation process. This process was executed in four steps: patch splitting, TVL1 optical-flow calculations, patch merging, and strain calculations. The patch splitting and merging steps followed the same procedure as in the denoising and contrast correction processes. The TVL1 optical-flow calculation was performed on all patch images using appropriate parameters to calculate the displacement of each pixel. Displacement calculations were performed only when the entire patch can be considered as a solid phase. The solid and liquid phases were distinguished with reference to the temperature distribution obtained by applying the two-color method to high-speed camera images. The strain values for each pixel were calculated from the displacement field after patch merging. The methods used to determine the appropriate parameters for the TVL1 optical flow and strain calculations are described in Sections 3.4 and 3.5, respectively.

By performing patch splitting and merging, the same machine learning model structure can be used even when the resolution or image size of the input images (original images) differs. The machine learning models for denoising and contrast correction were trained for each set of time-series in-situ images, that is, for each combination of resolution and welding conditions, allowing for adaptive image processing according to the acquisition conditions of the in-situ images.

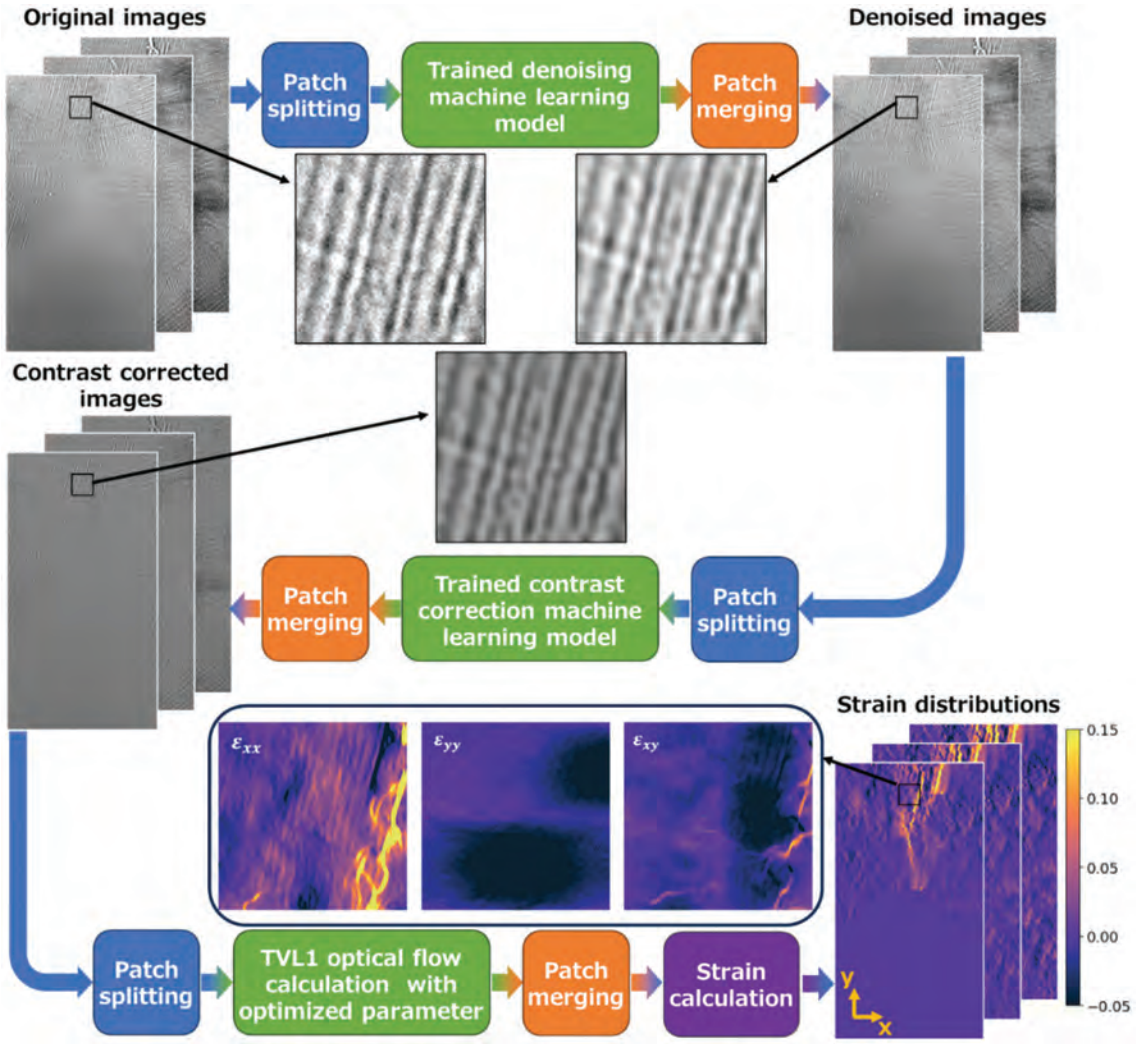

Figure 2. Overview of the proposed strain evaluation method. The upper row presents the denoising processing steps using a machine learning model. The middle row illustrates the contrast correction processing, also performed using a machine learning model. The lower row demonstrates the strain evaluation processing, which involves the calculation of the displacement field using the TVL1 optical flow, followed by the computation of the strain distribution from the displacement field.

3.2. Training method for the denoising of the machine learning model

The denoising machine learning model was trained based on the unsupervised learning approach proposed by Batson et al., known as Noise2Self [20]. The training framework for the denoising model is illustrated in Figure 4.

The input image patches for training were created by randomly extracting 128 × 128-pixel patches from the time series of in situ images obtained under a single acquisition condition. However, the image patches were only extracted from positions where the entire patch could be considered a solid phase. The model architecture adopted a structure common to general image processing models, consisting of an encoder part with convolutional layers, rectified linear unit (ReLU) activation layers, and maximum pooling layers; and a decoder part with convolutional, ReLU activation, and deconvolutional layers. The model parameters were updated based on the L_2 loss, which was calculated from the difference between the brightness values obtained by applying a donut-shaped smoothing kernel to set randomly the target pixels and the brightness value of the target pixels in the output image. During this process, data from nontarget pixels were excluded from the loss calculation. This loss calculation method is equivalent to the official implementation of the Noise2Self [21].

The training and validation datasets were constructed from the image patches extracted randomly from each frame, comprising five patches each. To optimize the model parameters, the AdamW algorithm (weight decay parameter: 10^{-5}, learning rate: 10^{-3}) was employed. Out of 1000 training steps, the L2 loss on the validation dataset was evaluated every 10 steps, and the model parameters with the smallest loss values were used as the training results.

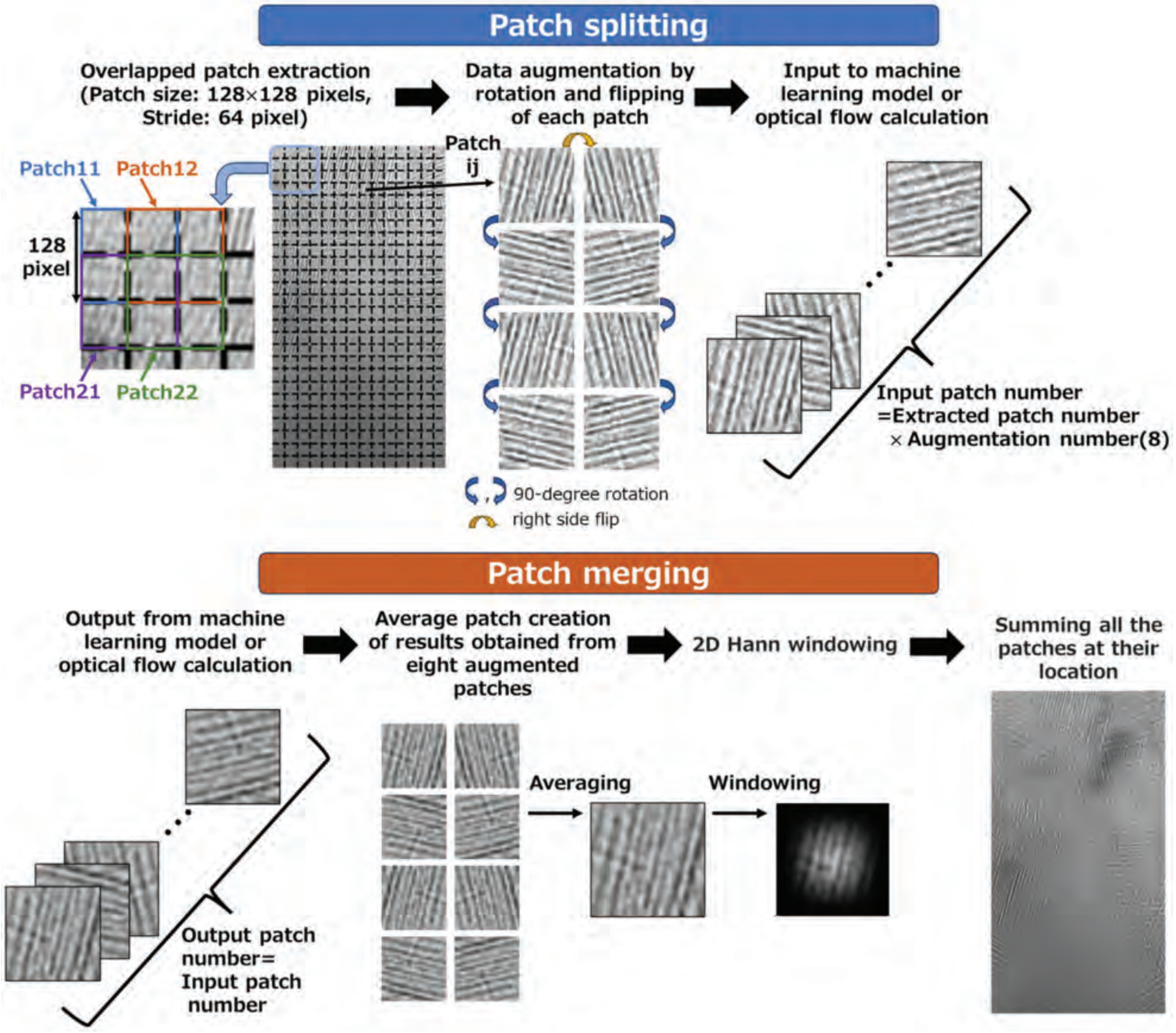

Figure 3. Patch splitting and merging procedure for denoising processing. The upper row demonstrates the process of splitting the original image into 128 × 128 pixel half-overlap patches and transforming these patches into mirror and rotationally symmetric images. The lower row illustrates the merging process where the patches are averaged and placed back into their original positions, followed by a Hann windowing process to reduce edge effects – inspired by the approach of Pielawski et al. [19] —and obtain the final image.

3.3. Training method for the contrast correction machine learning model

The training of the contrast correction machine learning model was conducted using the denoised images (i.e. the images after denoising processing) obtained under a single acquisition condition, as shown in Figure 2. The training framework for the contrast correction model is shown in Figure 5.

The method for obtaining the input image patches for training, as well as the construction of the training and validation datasets, followed the procedure described in Section 3.2. The architecture of the model is identical to that of the denoising model. The model parameters were updated based on the following loss function $loss_{cont}$

$$loss_{cont} = \frac{1}{n}\sum\{entr + (1 - SSIM)\} \quad (1)$$

where $entr$ represents the entropy of the output image, $SSIM$ is the structural similarity index measure [22] between the input and output image patches, and n is the number of samples in the dataset. By using Equation (1) as the loss function, the model achieves image processing that balances the reduction of brightness variation based on decreased $entr$ values and the preservation of the structure of the input image patches based on increased $SSIM$ values. Out of 1000 training steps, $loss_{cont}$ on the validation dataset was evaluated every 10 steps, and the model parameters with the smallest loss values were obtained as the training results.

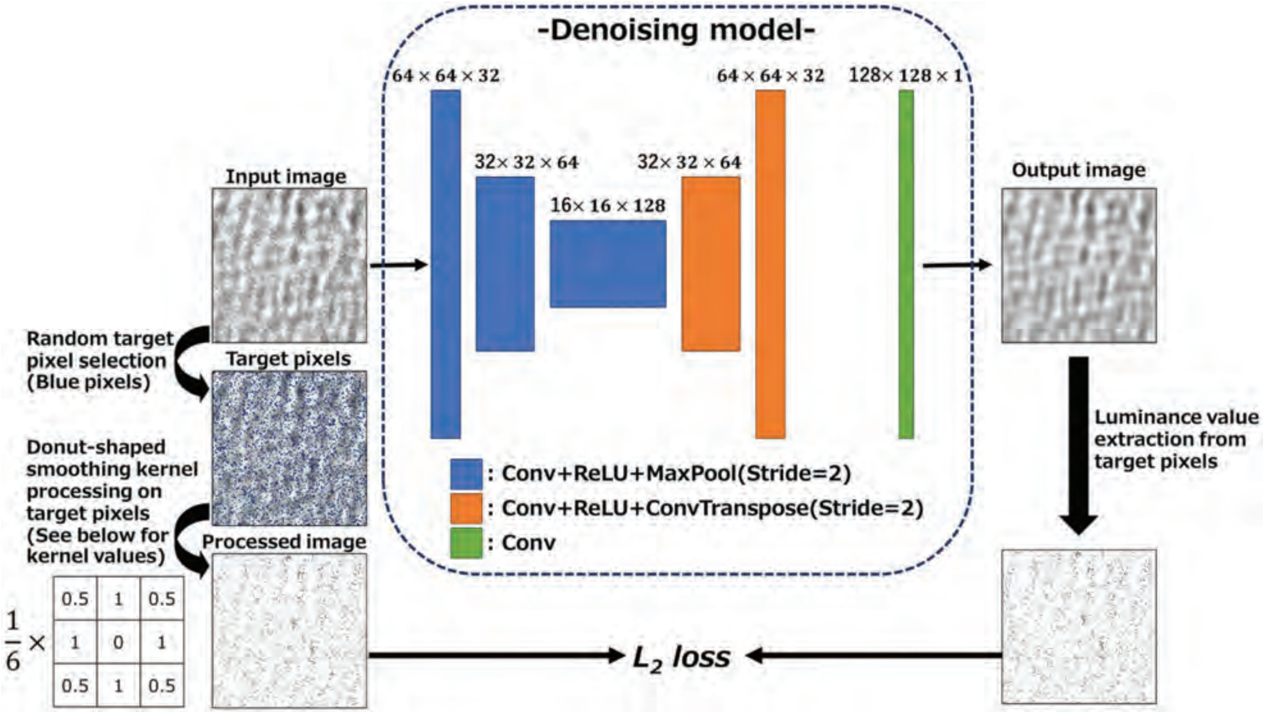

Figure 4. Framework of learning the denoising model. The denoising model was trained using a self-supervised approach inspired by Noise2Self [20]. The input image patches are extracted from in-situ observation images and processed through an encoder – decoder network to predict the denoised output. The model parameters are optimized using an L2 loss based on a donut-shaped smoothing kernel applied to randomly selected target pixels.

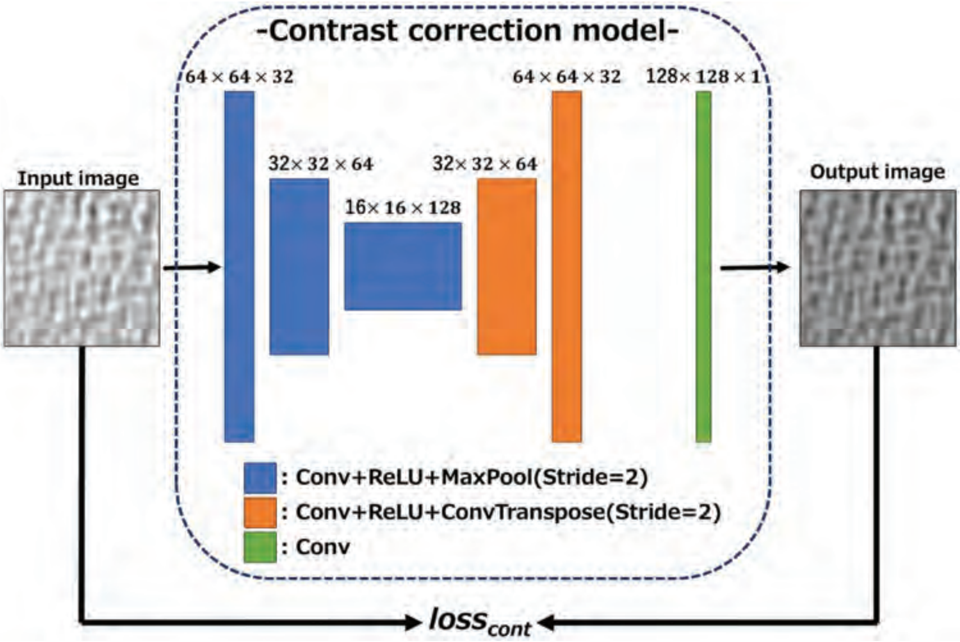

Figure 5. Framework of learning the contrast correction model. The contrast correction model was trained on denoised image patches. The model architecture is similar to that of the denoising model, and the loss function ($loss_{cont}$) combines the reduction of output image entropy and the increase of structural similarity index measure between input and output patches, ensuring both contrast correction and structural preservation.

3.4. Method for searching optimal parameters for TVL1 optical-flow calculation

The search for the optimal parameters in the TVL1 optical flow was conducted on contrast-corrected images obtained under a single acquisition condition, that is, the contrast-corrected images shown in Figure 2. The method used to obtain input image patches for parameter optimization is essentially the same as that described in Section 3.2; however, owing to the computational time constraints, one image patch was randomly extracted from each frame, and the optical flow to the image patch was calculated at the same position in the subsequent frame.

As stated by Zach et al., the parameter that has the most significant impact on the results of the TVL1 optical-flow calculation is the attachment parameter λ [12]. This parameter controls the smoothness of the resulting displacement field and should be adjusted according to the evaluation target images.

The optimal value of this attachment parameter was determined using the framework shown in Figure 6. Specifically, the forward displacement from time t to time $t+1$ for each pixel was calculated as u_f and v_f for the x- and y-directions, respectively, and the backward displacement from time $t+1$ to time t was calculated as u_b and v_b for the x- and y-directions, respectively. Considering that under ideal conditions, $u_f + u_b$ and $v_f + v_b$ should each be zero, the following loss function, $loss_{disp}$, was defined, and the optimal attachment parameter that minimized $loss_{disp}$ was searched for.

$$loss_{disp} = \frac{1}{n}\sum\left[\left\{\frac{\left(u_f + u_b\right)^2}{u_f^2 + u_b^2}\right\} + \left\{\frac{\left(v_f + v_b\right)^2}{v_f^2 + v_b^2}\right\}\right] \tag{2}$$

The TVL1 optical-flow calculation was performed using the optical_flow_tvl1 function from the Python image-processing library scikit-image [23]. Parameters other than the attachment parameter were fixed with the following settings (tightness = 0.3, num_warp = 50, num_iter = 10, and prefilter = True). Parameters other than the attachment parameter were fixed with the following settings: tightness = 0.3, num_warp = 50, num_iter = 10, and prefilter = True. The values of tightness and num_iter were set to their default values. The value of num_warp was chosen to be sufficiently large to ensure stable computation results, and the prefilter was set to True to stabilize the calculations. The minimize-scalar function from the Python numerical processing library Scipy [24] was used to search for the optimal attachment parameters. The optimal attachment parameter was determined using the Brent algorithm within the range of $\lambda = (0.1, 10)$.

3.5. Strain calculation method

Strain calculations were performed on the displacement fields obtained for each frame until the patch-merging step, as shown in the lower part of Figure 2. Specifically, using the displacement fields for each frame, the total displacement from the initial image to each frame was determined; from this total displacement, the strain field for each frame was calculated.

To calculate the total displacement, the nodes were placed at all the pixel positions in the initial image (time $t = 0$, assuming zero strain). Let the number of pixels in the vertical and horizontal directions be denoted by H and W, respectively, and let the node number in the ith row and jth column be ij. The initial x-coordinate x_{ij}^0 and y-coordinate y_{ij}^0 of the ijth node are given by

$$x_{ij}^0 = j, y_{ij}^0 = i(i = 1, \cdots H, j = 1, \cdots W) \tag{3}$$

Using the x- and y-displacement fields u^t and v^t for each frame at time t, the x- and y-coordinates x_{ij}^t and y-coordinate y_{ij}^t of each node at time t were calculated using the following equations,

$$x_{ij}^t = x_{ij}^0 + \sum_{t=1}^{t} u^t\left(x_{ij}^t, y_{ij}^t\right), y_{ij}^t = y_{ij}^0 + \sum_{t=1}^{t} v^t\left(x_{ij}^t, y_{ij}^t\right), \tag{4}$$

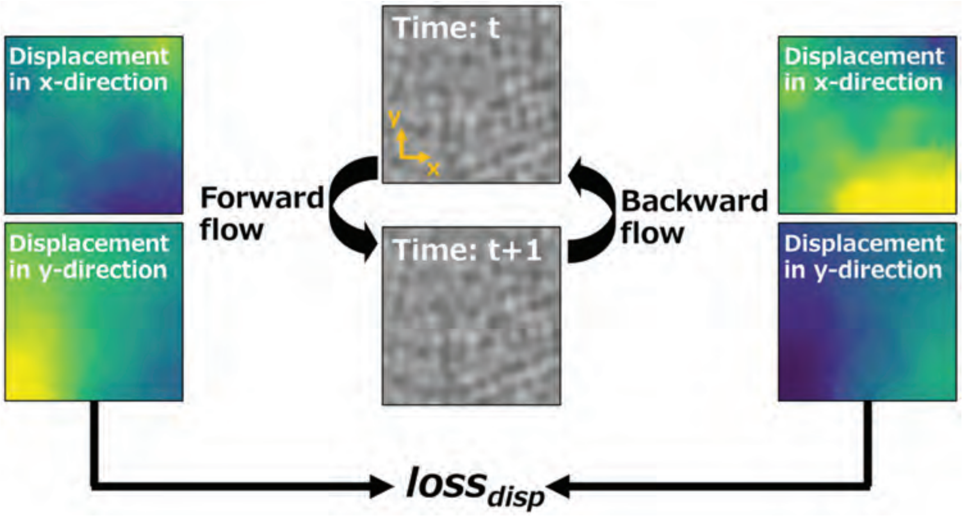

Figure 6. Framework used to optimize the attachment parameter (λ) for TVL1 optical-flow calculation. The optimal attachment parameter was determined by minimizing the loss function ($loss_{disp}$), which evaluated the discrepancy between forward and backward displacement fields. The forward displacement (u_f, v_f) was calculated from time t to $t+1$, and the backward displacement (u_b, v_b) from time t + 1 to t. The goal was to achieve $u_f + u_b \approx 0$ and $v_f + v_b \approx 0$ for accurate strain evaluation.

where u^t and v^t were calculated at noninteger values (x^t_{ij}, y^t_{ij}) by interpolation using cubic spline functions. Using $x^0_{ij}, y^0_{ij}, x^t_{ij}$, and y^t_{ij}, the total displacements U^t and V^t in the x- and y-directions from time 0 to t were calculated as follows,

$$U^t = x^t_{ij} - x^0_{ij},\ V^t = y^t_{ij} - y^0_{ij} \tag{5}$$

For strain field calculations, the in-plane strains $(\varepsilon_{xx})^t_{ij}$, $(\varepsilon_{yy})^t_{ij}$, and $(\varepsilon_{xy})^t_{ij}$ at each node at time t were obtained using the following equations,

$$\varepsilon^t_{xx} = \frac{\partial U^t}{\partial x},\ \varepsilon_{yy} = \frac{\partial V^t}{\partial y},\ \varepsilon_{xy} = \frac{1}{2}\left\{\frac{\partial U^t}{\partial y} + \frac{\partial V^t}{\partial x}\right\} \tag{6}$$

The partial derivatives of the equations were calculated using a 5-point finite difference method. Because of the observed displacement discontinuities in the regions divided by the solid-liquid interface after solidification, differences across regions were not calculated, and one-sided differences were used. One-sided differences were used at image edges, whereas central differences were used elsewhere.

3.6. Effectiveness validation method of the proposed method

Figure 7 shows the validation method of the effectiveness of the proposed strain evaluation method. The effectiveness was validated by evaluating the x-direction strain $\varepsilon^{l_1 l_2}_{xx}(y)$ occurring between the evaluation lines L_1 (x-coordinate: x_1) and L_2 (x-coordinate: x_2) at each y-coordinate $(y_1 \leq y \leq y_2)$ as time progresses from t_1 to t_2 within the time range in which the entire field of view is in the solid phase. The evaluation was performed using two methods, and the results were compared.

The first method used the strain distribution obtained from the proposed strain evaluation method. In this method, $\varepsilon^{l_1 l_2}_{xx}(y)$ is calculated as the average strain between the evaluation lines L_1 and L_2. Specifically, it is calculated from the x-direction strain distribution $\varepsilon^{t_1}_{xx}$ at time t_1 and $\varepsilon^{t_2}_{xx}$ at time t_2 using the following equation,

$$\left\{\varepsilon^{l_1 l_2}_{xx}(y)\right\}_1 = \frac{1}{x_2 - x_1}\sum_{x=x_1}^{x_2}\left\{\varepsilon^{t_2}_{xx}(x) - \varepsilon^{t_1}_{xx}(x)\right\} \tag{7}$$

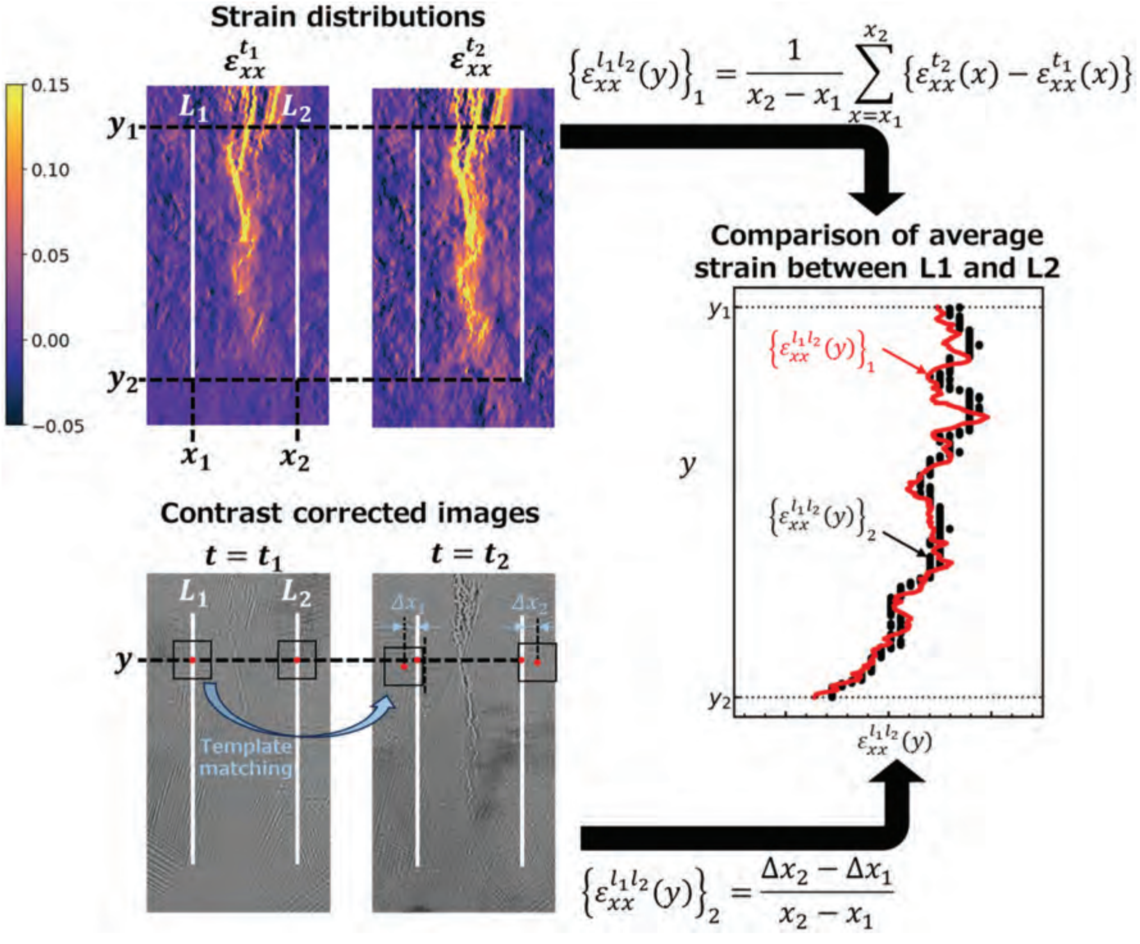

Figure 7. Overview of the validation method for the proposed strain evaluation technique. The x-direction strain between evaluation lines L_1 (x-coordinate: x_1) and L_2 (x-coordinate: x_2) at various y-coordinates ($y_1 \leq y \leq y_2$) was assessed as time progressed from t_1 to t_2. Two methods were used for this evaluation: the proposed strain evaluation and the template matching. The results from both methods were compared to validate the effectiveness of the proposed technique.

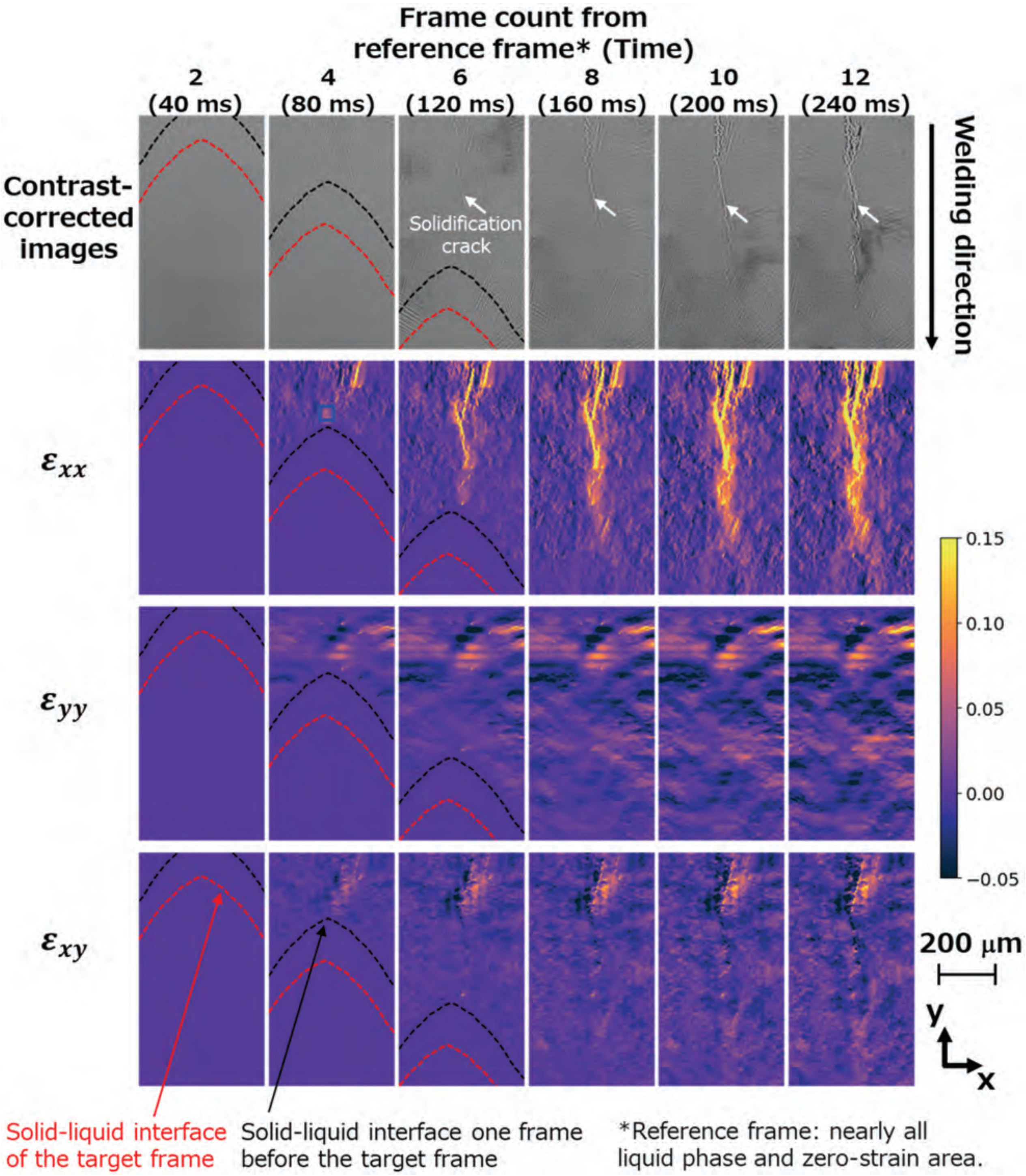

Figure 8. Strain distributions evaluated using the proposed method. The red-dashed lines indicate the solid – liquid interface determined by the two-color method, while the black-dashed lines show the solid – liquid interface from the previous frame (test 1; welding speed: 10 mm/s, resolution: 0.5 μm/pixel, frame rate: 50 frames/s).

The second method uses template matching. In this method, a square template is extracted from the image at time t_1, and its position at time t_2 is evaluated to calculate the average strain between the evaluation lines L_1 and L_2. The average strain $\left\{\varepsilon_{xx}^{l_1 l_2}(y)\right\}_2$ between the evaluation lines L_1 and L_2 at a specific y-coordinate is calculated using the x-direction displacements Δx_1 and Δx_2 of two templates with center y-coordinates at y and center x-coordinates at x_1 and x_2, respectively, using the following equation,

$$\left\{\varepsilon_{xx}^{l_1 l_2}(y)\right\}_2 = \frac{\Delta x_2 - \Delta x_1}{x_2 - x_1} \tag{8}$$

Template matching was performed using the matchTemplate function of the Python image processing library opencv [25]. The normalized correlation coefficient was used for the similarity calculation. The template size was set to 40 × 40 pixels for the high-resolution images (Tests 1 and 2) and 20 × 20 pixels for the low-resolution images (Test 3). The search

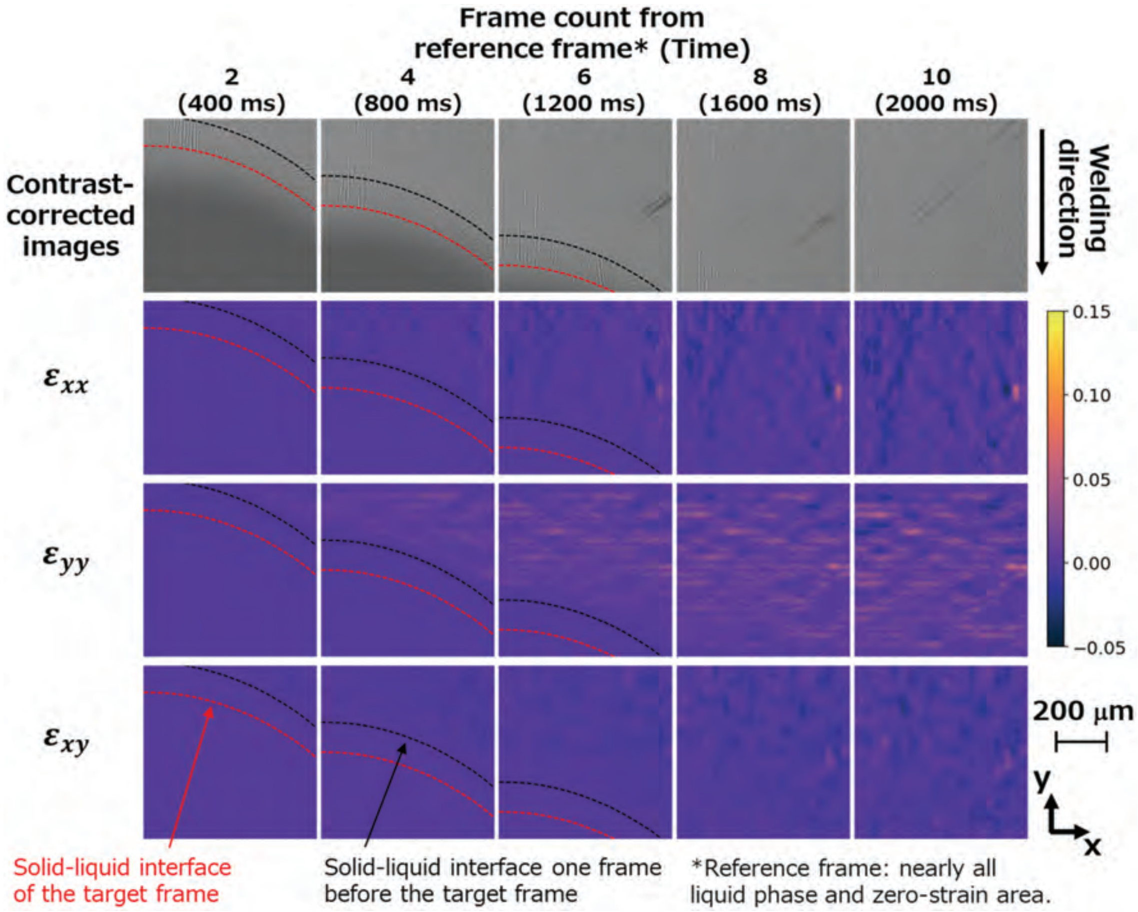

Figure 9. Strain distributions evaluated by the proposed method (test 2; welding speed: 1 mm/s, resolution: 0.5 μm/pixel, frame rate: 5 frames/s).

range was set to ± 50 pixels from the template acquisition center position for high-resolution images and to ± 25 pixels for low-resolution images. To improve the resolution of strain distribution, template matching was applied to high-resolution images obtained by threefold interpolation of time-series images after contrast correction, that is, contrast-corrected images in Figure 2. The positions of evaluation lines L_1 and L_2 varied depending on the acquisition conditions of the in-situ observation images, as will be described later.

4. Results and discussion

4.1. Strain evaluation results

Figures 8, 9, and 10, show the distributions of in-plane strains ε_{xx}, ε_{yy}, and ε_{xy} obtained by the proposed strain evaluation method for selected frames (every 40 ms in the cases of Tests 1 and 3 and every 400 ms in the case of Test 2), along with the contrast-corrected images. Contrast-corrected images and in-plane strain for all frames in all test cases are shown in the supplemental videos. In addition, for the observation fields, Tests 1 and 3 had the welding area centered near the middle of the image, whereas Test 2 had the welding area centered near the left edge of the image. Here, the reference frame (Frame count: 0, Time: 0 ms) is a frame where almost the entire field of view is in the liquid phase, with the strain set to zero throughout.

In the figures, the red-dotted lines indicate the solid – liquid interface of each frame determined with reference to the temperature distribution obtained by the two-color method, whereas the black-dotted lines show the solid – liquid interface from the previous frame. The TVL1 optical-flow calculation was performed only when the entire area of the patch image of the previous and current frames can be considered as the solid phase, assuming zero displacements in the other areas. Therefore, if the patch acquisition area included regions below the black-dotted line (in the direction of weld progression), all strains were calculated to be zero. This is why the strain is zero near the solid – liquid interface, even in regions that appear solid in the contrast-corrected images.

From the results in Figure 8, it can be observed that solidification cracking occurred in Test 1. In these conditions, large tensile strain ε_{xx} in the weld width direction occurs in the region where solidification cracking occurs (with values exceeding 0.15). ε_{yy} and ε_{xy} do not show prominent strain concentrations as those of ε_{xx}. This is because the opening direction of the solidification crack was in the x-direction (weld

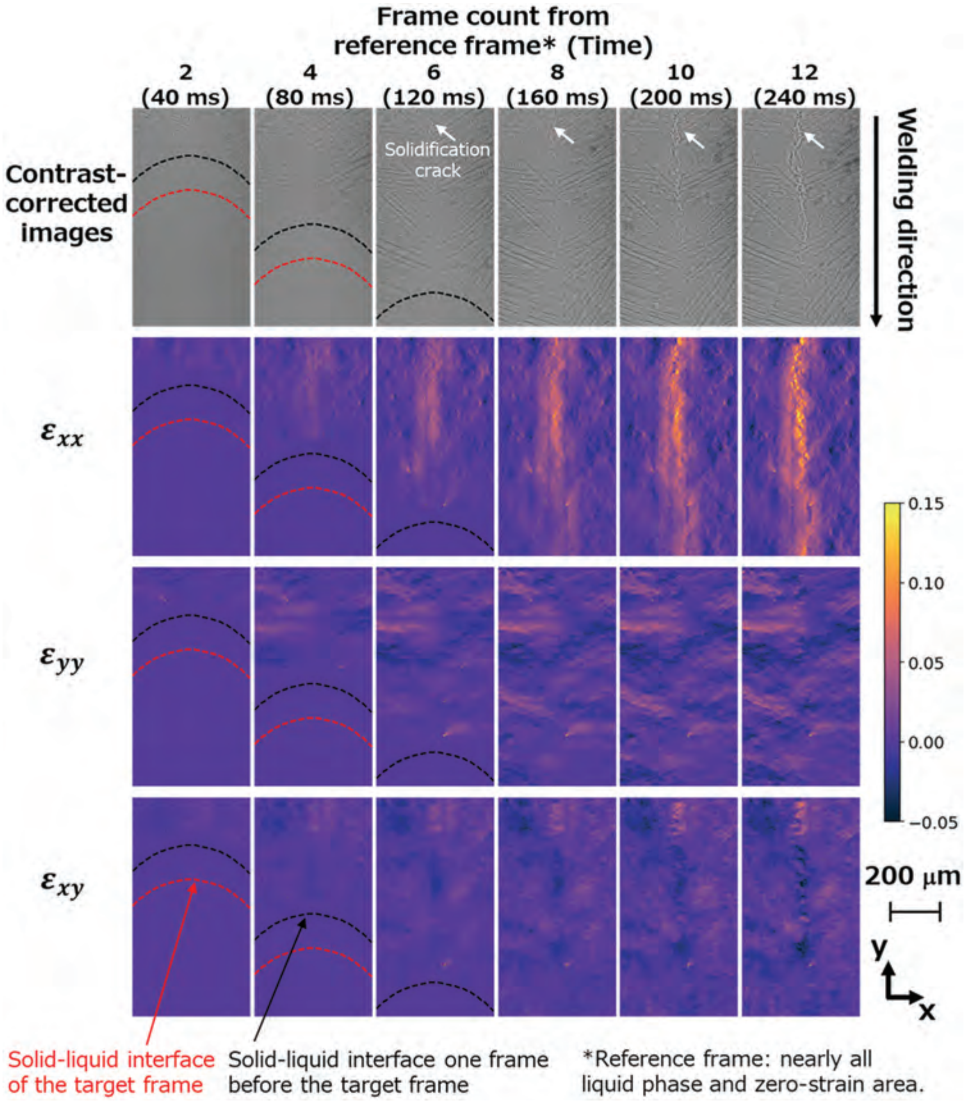

Figure 10. Strain distributions evaluated by the proposed method (test 3; welding speed: 10 mm/s, resolution: 1.1 µm/pixel, frame rate: 50 frames/s).

width direction). Additionally, the blue rectangular area in frame 4 is a region wherein there was not a distinct solidification crack at that time; however, it appeared two frames later. In other words, ε_{xx} in the blue rectangular area represents the approximate strain value just before solidification cracking occurs with an approximate average of 0.028 within that region. The lower limit of the strain at which solidification cracking occurs in austenitic stainless steel with high Cr and Ni contents, similar to the alloy used in this study, is in the range of 0.02–0.09 [1,26]. This indicates the validity of the strain distribution obtained using the proposed method.

Figure 9 shows that no distinct cracks are observed over the entire time under the conditions of Test 2. Under these conditions, no distinct strain concentrations were observed. Additionally, the in-plane average strains $(\varepsilon_{xx})_{ave}$, $(\varepsilon_{yy})_{ave}$, and $(\varepsilon_{xy})_{ave}$ across the entire field of view in frame count 10 are approximately equal to −0.005, 0.004, and −0.003, respectively. These values are consistent with conventional knowledge that in cases where no cracks occur, the strain in the weld width direction (x-direction strain) and shear strain are typically smaller than the strain in the weld direction (y-direction strain) [27].

The results in Figure 10 show strain distributions similar to those in Figure 8, which were obtained under the same welding conditions using high-resolution images. In both cases, the strain in the weld width direction in the area where solidification cracking occurs is approximately equal to 0.15. This suggests that the proposed strain evaluation method can appropriately evaluate the strain regardless of the resolution of the in-situ observation images.

As described above, using the proposed strain evaluation method on time-series in-situ images captured under three different conditions produced consistent strain distributions and strain histories that matched existing knowledge.

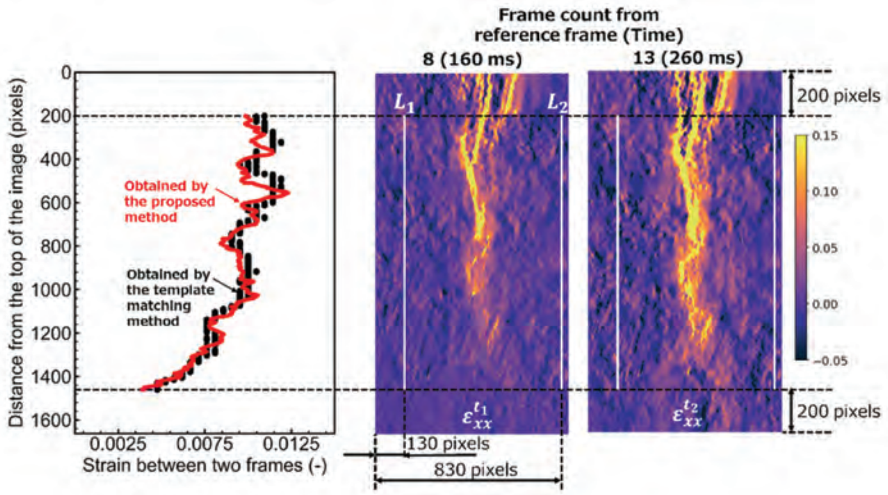

(a) Test 1; welding speed: 10 mm/s, resolution: 0.5 µm/pixel, frame rate: 50 frames/s

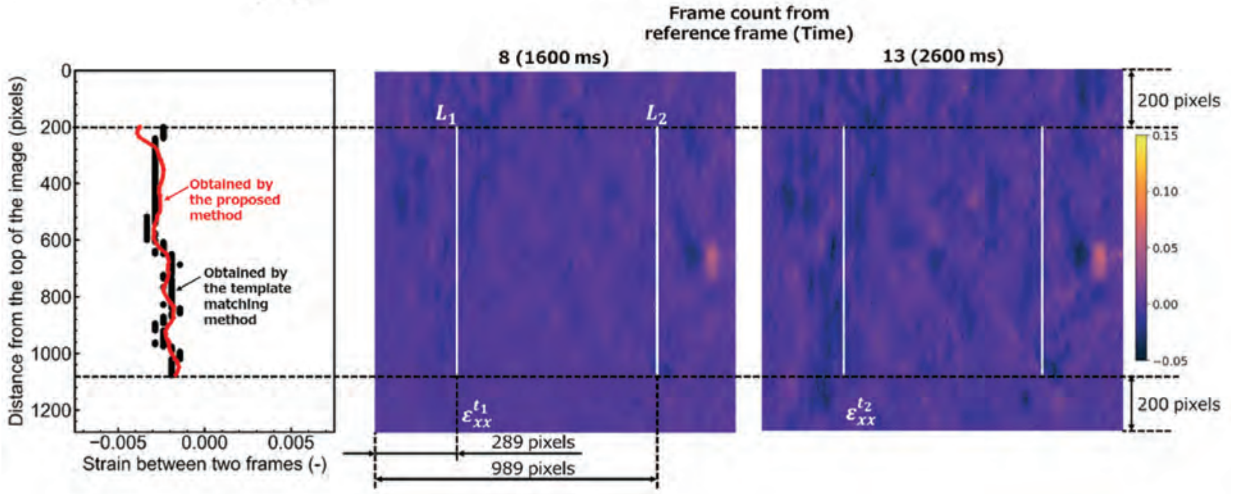

(b) Test 2; welding speed: 1 mm/s, resolution: 0.5 µm/pixel, frame rate: 5 frames/s

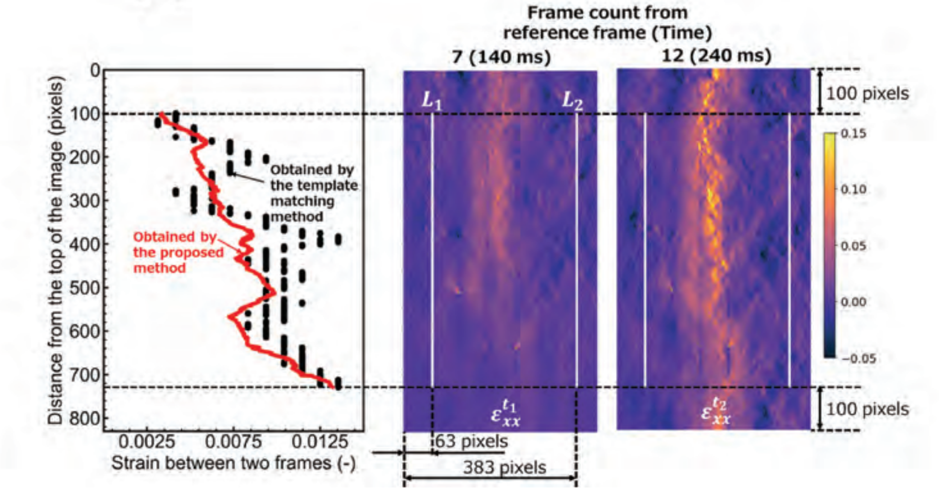

(c) Test 3; welding speed: 10 mm/s, resolution: 1.1 µm/pixel, frame rate: 50 frames/s

Figure 11. Comparisons of the x-direction strain (ε_{xx}) between evaluation lines L_1(x-coordinate: x_1) and L_2 (x-coordinate: x_2) at various y-coordinates ($y_1 \leq y \leq y_2$), evaluated using the proposed and template matching methods.

4.2. Validation results of effectiveness

Figure 11 shows the x-direction strain $\varepsilon_{xx}^{l_1 l_2}(y)$ between evaluation lines L_1 (x-coordinate: x_1) and L_2 (x-coordinate: x_2) at each y-coordinate ($y_1 \leq y \leq y_2$) as time progresses from t_1 to t_2, calculated using the two methods described in Section 3.6. In this case, the $\varepsilon_{xx}^{l_1 l_2}(y)$ value for Test 2 has a smaller value compared with the other conditions; thus, the horizontal axis of the graph is different. In addition, each figure shows the dimensions, frame count, and time required for the calculation of x_1, x_2, y_1, y_2, t_1, and t_2. The values of x_1 and x_2 were determined such that the solidification crack region was approximately in the middle between the evaluation lines for Tests 1 and 3, where solidification cracking occurred, and centered on the image width direction for Test 2. The distance between the evaluation lines was set to 700 pixels for the high-resolution images and to 320 pixels for the low-resolution images (considering the resolution ratio needed to make the actual distance almost the same as that for the high-resolution images). The values of y_1 and y_2 were set to 200 pixels from the top and bottom edges of the image for high-resolution images and to 100 pixels for low-resolution images. For t_1 and t_2, t_1 was set based on the frame in which the strain was first calculated for the entire field of view, and t_2 was set to five frames after t_1.

The figures show that for all tests, the average strain between L_1 and L_2 obtained by the proposed strain evaluation method closely matched the strain obtained by the template-matching method. The template-matching method has limitations in calculating the strain distribution of all the pixels within the field of view and is constrained by the resolution of the evaluation values to the distance between points (distance between L_1 and L_2). However, because the strain was calculated based on the correlation of brightness values within the template, the calculated results were considered to have a certain level of accuracy. These results indicate the effectiveness of the proposed strain evaluation method.

The strains in Tests 1 and 3, calculated from in-situ images at different resolutions but under the same welding conditions, vary within a similar range centered at approximately 0.0075. Because of the uncertainty in the occurrence and progression behavior of solidification cracking, they do not completely match. However, similar strain evaluation results for the same welding conditions further emphasize the effectiveness of the proposed strain evaluation method.

In conclusion, the proposed strain evaluation method is useful because it can be applied using the same procedure, even if the acquisition conditions of the time-series in-situ observation images (such as welding conditions and image resolution) change. The proposed method is considered superior because it eliminates the need for adjusting image processing parameters, which is required in classical image processing methods. Additionally, by adopting optical flow calculation instead of DIC, the proposed method is less affected by the presence of liquid phases within the field of view. The evaluation results from the proposed method were compared with the quantitative evaluation results from the template matching method, and it was confirmed that comparable global strains were obtained. Unlike the template-matching method, which only provides strain between markers, the proposed method offers strain evaluation for each pixel, allowing for a more detailed analysis of the strain distribution and history.

5. Conclusions

In this study, a new strain evaluation method using time-series in-situ images was proposed as an additional application of the high-brightness, synchrotron X-ray, in-situ technology developed to understand the solidification process of welds. The conclusions are summarized as follows:

(1) A strain distribution and strain history evaluation method for weld solidification zones was proposed by combining denoising and contrast correction using machine learning models with the TVL1 optical-flow calculation method. This method can be implemented using the same procedure regardless of different welding conditions or image resolutions and has the advantage of not requiring parameter settings for optical-flow calculation.

(2) The results obtained using the proposed method allowed detailed observations of strain distribution changes owing to differences in welding conditions and the presence or absence of solidification cracking. The evaluation results correspond to conventional knowledge and confirm consistent strain distributions and strain histories.

(3) The strain distributions obtained using the proposed method matched well those obtained using the template matching method, demonstrating the reliability and effectiveness of the proposed method.

The method developed in this study is expected to become a new tool for deepening our understanding of solidification cracking, residual stress, and residual deformation in welding technology, thereby contributing significantly to the advancement of welding process control. Future applications of the proposed method include quantitative evaluations of the relationships between the microstructure, temperature, and strain in areas where solidification cracks form. These applications can help understand the solidification cracking phenomenon in detail and to explore ways to prevent solidification cracks. In addition, the proposed method is expected to be applied to the evaluation of three-dimensional metal printing processes that have recently gained attention.

Future challenges include the examination of the applicability of this method to various materials under a broad range of welding conditions. Additionally, it is important to advance research aimed at practical applications in the production of welded structures, such as the development of welding technology for manufacturing seismic dampers using the alloys employed in this study.

Disclosure statement

No potential conflict of interest was reported by the author(s).

Funding

This research was partially supported by Grants-in-Aid for Scientific Research (KAKENHI) [grant numbers JP24K01220 and JP23H01731] from the Japanese Society for the Promotion of Science. Japan Society for the Promotion of Science [JP24K01220]; Japan Society for the Promotion of Science [JP23H01731].

ORCID

Houichi Kitano http://orcid.org/0000-0002-0778-574X
Fumiyoshi Yoshinaka http://orcid.org/0000-0003-0534-7815
Takahiro Sawaguchi http://orcid.org/0000-0002-9405-002X

References

[1] Coniglio N, Cross CE. Initiation and growth mechanisms for weld solidification cracking. Int Mater Rev. 2013;58(7):375–397. doi: 10.1179/1743280413Y.0000000020
[2] Matsunawa A, Mizutani M, Katayama S, et al. Porosity formation mechanism and its prevention in laser welding. Weld Int. 2003;17(6):431–437. doi: 10.1533/wint.2003.3138
[3] Molak RM, Paradowski K, Brynk T, et al. Measurement of mechanical properties in a 316L stainless steel welded joint. Int J Press Vessels Pip. 2009;86(1):43–47. doi: 10.1016/j.ijpvp.2008.11.002
[4] Tweed JH, Knott JF. Micromechanisms of failure in C-Mn weld metals. Acta Metallurgica. 1987;35(7):1401–1414. doi: 10.1016/0001-6160(87)90087-3
[5] Nagira T, Nakamura T, Yoshinaka F, et al. Direct observation of solidification behaviors of Fe-mn-si alloys during TIG spot welding using synchrotron X-ray. Scr Materialia. 2022;216:114743. doi: 10.1016/j.scriptamat.2022.114743
[6] Nagira T, Yamashita D, Kamai M, et al. Time-resolved X-ray imaging of solidification cracking for Al-Cu alloy at the weld crater. Mater Charact. 2020;167:110469. doi: 10.1016/j.matchar.2020.110469
[7] Nagira T, Yamashita D, Kamai M, et al. In situ observation of solidification crack propagation for type 310S and 316L stainless steels during TIG welding using synchrotron X-ray imaging. J Mater Sci. 2021;56(17):10653–10663. doi: 10.1007/s10853-021-05969-0
[8] Tomasi C, Manduchi R. Bilateral filtering for gray and color images. In: Sixth International Conference on Computer Vision (IEEE Cat. No. 98CH36271); Bombay, India. IEEE; 2016. p. 839–846.
[9] Pizer SM, Amburn EP, Austin JD, et al. Adaptive histogram equalization and its variations. Comput Vision, Graphics, Image Process. 1987;39(3):355–368. doi: 10.1016/S0734-189X(87)80186-X
[10] Pan B. Recent progress in digital image correlation. Exp Mech. 2011;51(7):1223–1235. doi: 10.1007/s11340-010-9418-3
[11] Wedel A, Pock T, Zach C, et al. An improved algorithm for TV-L1 optical flow. In: Cremers D, Rosenhahn B, Yuille AL, Schmidt FR, editors. Statistical and geometrical approaches to visual motion analysis. Berlin, Heidelberg: Springer; 2009. p. 23–45.
[12] Zach C, Pock T, Bischof H. A duality based approach for realtime TV-L1 optical flow. In: Pattern recognition: 29th DAGM Symposium. Heidelberg, Germany: Springer; 2007 Sep 12-14. p. 214–223.
[13] Kai B, Uwe DH. Template matching using fast normalized cross correlation. Optical Pattern Recognit XII. 2001;4387:95–102.
[14] Nagashima N, Yoshinaka F, Sawaguchi T. Study on extremely-low-cycle fatigue of Fe–15Mn–10Cr–8Ni–4Si alloy. Mater Trans. 2023;64(2):548–554. doi: 10.2320/matertrans.MT-Z2022018
[15] Nagira T, Nakamura T, Sawaguchi T, et al. Friction stir welding of Fe-15Mn-10Cr-8Ni-4Si seismic damping alloy. ISIJ Int. 2023;63(12):2056–2065. doi: 10.2355/isijinternational.ISIJINT-2023-305
[16] Sawaguchi T, Tomota Y, Yoshinaka F, et al. Evidence supporting reversible martensitic transformation under cyclic loading on Fe–mn–si–al alloys using in situ neutron diffraction. Acta Materialia. 2023;242:118494. doi: 10.1016/j.actamat.2022.118494
[17] Yoshinaka F, Sawaguchi T, Takamori S, et al. Transformation-induced plasticity via γ → ε → α' and γ → ε → γ martensitic transformations in Fe–15Mn–10Cr–8Ni–4Si alloy. Mater Sci Eng: A. 2022;833:142583. doi: 10.1016/j.msea.2021.142583
[18] Abe D, Matsuzaka F, Murakami Y, et al. Determining the BTR by conducting a trans-varestraint test using a high-speed camera and two-color pyrometry. Weld World. 2018;62(6):1237–1246. doi: 10.1007/s40194-018-0608-4
[19] Pielawski N, Wählby C, Zhang J. Introducing Hann windows for reducing edge-effects in patch-based

image segmentation. PLOS ONE. 2020;15(3): e0229839. doi: 10.1371/journal.pone.0229839

[20] Batson JD, Royer LA. Noise2Self: blind denoising by self-supervision. International Conference on Machine Learning; Bombay, India; 2019 Jan 9–15. p. 524–533.

[21] Noise2Self: Blind Denoising by Self-supervision. Available from: https://github.com/czbiohub-sf/noise2self

[22] Zhou W, Bovik AC, Sheikh HR, et al. Image quality assessment: from error visibility to structural similarity. IEEE Trans Image Process. 2004;13 (4):600–612. doi: 10.1109/TIP.2003.819861

[23] skimage.registration.optical_flow_tvl1. Available from: https://scikit-image.org/docs/stable/api/skimage.registration.html#skimage.registration.optical_flow_tvl1

[24] scipy.optimize.minimize_scalar. Available from: https://docs.scipy.org/doc/scipy/reference/generated/scipy.optimize.minimize_scalar.html

[25] cv2.matchTemplate. Available from: https://docs.opencv.org/4.x/df/dfb/group__imgproc__object.html#ga586ebfb0a7fb604b35a23d85391329be

[26] Matsuda F, Nakagawa H, Nakata K, et al. Quantitative evaluation of solidification brittleness of weld metal during solidification by means of in-situ observation and measurement (report I: development of the MISO technique (materials, metallurgy & weldability). Trans JWRI. 1983;12(1):65–72.

[27] Wang L, Li K, Sanusei S. Strain decoupling for the real time strains measured during welding process. Advancement Optical Methods Exp Mech. 2014;3:369–377. Springer International Publishing.